Interfacial instability and transition of jetting and dripping modes in a co-flow focusing process Ⓕ

ⓘⒹ **Kai Mu** (穆恺), ⓘⒹ **Ran Qiao** (乔然), ⓘⒹ **Ting Si** (司廷), **et al.**

COLLECTIONS

Ⓕ This paper was selected as Featured

View Online   Export Citation   CrossMark

ARTICLES YOU MAY BE INTERESTED IN

Experimental and numerical investigations on interface coupling of coaxial liquid jets in co-flow focusing
Physics of Fluids **32**, 042103 (2020); https://doi.org/10.1063/5.0002102

Instability and interface coupling of coaxial liquid jets in a driving stream
Physics of Fluids **32**, 092107 (2020); https://doi.org/10.1063/5.0018279

Manipulation of jet breakup length and droplet size in axisymmetric flow focusing upon actuation
Physics of Fluids **31**, 091702 (2019); https://doi.org/10.1063/1.5122761

33, 052118

Interfacial instability and transition of jetting and dripping modes in a co-flow focusing process ⓕ

View Online   Export Citation   CrossMark

Kai Mu (穆恺),[1] ⓘ Ran Qiao (乔然),[1] ⓘ Ting Si (司廷),[1,a] ⓘ Xueqin Cheng (程学勤),[2] and Hang Ding (丁航)[1]

AFFILIATIONS

[1]Department of Modern Mechanics, University of Science and Technology of China, Hefei 230026, China
[2]Shenzhen Shanshuile Environmental Protection Technology Co., Ltd., Shenzhen 518172, China

[a]Author to whom correspondence should be addressed: tsi@ustc.edu.cn

ABSTRACT

The breakup dynamics of coaxial liquid interfaces into compound droplets in a co-flow focusing process is studied systematically. In experiments, the jetting and dripping modes downstream the focusing orifice are identified within the parametric regime where a coaxial liquid cone can be established steadily, and the phase diagram is plotted under different flow rates of inner, outer, and driving liquids. The force balance for the jet interface is analyzed numerically to explore the critical conditions for the jetting-dripping transition. It is found that the instability of the inner interface is much easier to trigger the modes transition, and the transition criterion is decided by the balance of inertia force, shear stress, and interfacial tension at the local inner jet. The linear spatiotemporal instability analysis is further carried out to study the convective and absolute instabilities of the coaxial jets. The effects of main process parameters on jet instability are accessed, and the boundary between the absolute/convective instabilities is further compared with the experimental and numerical results, which achieves good agreement. Finally, the energy budget analysis of the instability of coaxial liquid jets is performed to provide more understanding of physical mechanisms for the mode transition.

I. INTRODUCTION

Microcapsules have been widely used in various scientific and engineering applications due to their multi-layered structures comprising core materials which are encapsulated in a single shell sized at micrometer scales. In recent decades, advanced microencapsulation techniques have drawn more and more attention. In particular, capillary flows are capable of stretching fluids into thin liquid jets, resulting in droplets with satisfactory morphologies and structures.[1,2] In this work, we mainly focus on one typical capillary flow called flow focusing, in which two phases of immiscible fluids flow through a confined orifice with their interface stretched to micrometer scales and finally disintegrated to compound droplets in a boundless open space.[3,4] When triple phases of fluids flow through the orifice synchronously, a steady co-flowing cone-jet configuration for the focused core and shell fluids can be formed under the hydrodynamic forces of outermost driving fluid, named co-flow focusing (CFF).[5–9] In comparison with the most commonly used microfluidic methods such as two-dimensional PDMS (polydimethylsiloxane) microchannels and axisymmetric glass microcapillaries,[10–13] the CFF can reduce the wetting effect of channel walls and often operates at relatively high Reynolds numbers with high-efficient production of compound droplets, implying that the inertia force mainly dominates the flow instability.

In the single-axial flow focusing, various flow modes have been identified,[14] in which the jetting and dripping modes are two typical ones that are often used to produce microdroplets.[15,16] In the jetting mode, a thin liquid jet can be formed downstream the focusing orifice with droplets generated at the end of the jet; while in the dripping mode, the droplets are usually formed just at the exit of the focusing orifice. Generally, the jetting mode can generate microdroplets with their size similar to the jet diameter under relatively high frequency; while the dripping mode produces droplets with larger size and better uniformity than those in the jetting mode.[14] In recent studies, the external excitations are applied to manipulate the breakup of liquid jets, able to enhance the droplet uniformity, and realize the active generation of microdroplets in the jetting mode.[17,18]

In the pioneering investigation on CFF, the coaxial liquid jets and double emulsions were produced in unbounded surrounding gas.[3] Then the morphologies of multiple coaxial jets under different flow rates of inner and outer liquid jets were revealed by experiments, either for coaxial gas–liquid jets[19] or liquid–liquid jets.[5] Recent studies have

focused on the interface coupling manner of inner and outer jets as their diameter ratio varies, which are further compared with the simplified single jet models as the inner to outer diameter ratio of coaxial jets approaches 0 or 1.[8] Numerical simulations have been also performed to provide the breakup dynamics of coaxial jets under different coupling manners, illustrating the flow field details which are difficult to be obtained in experiments.[7] The effects of liquid flow rates, physical properties, and device geometry on the formation of compound droplets have also been accessed numerically.[20–23]

The instability theory is a powerful tool to study the growth of disturbances on the jet interface.[24] Previous theoretical studies on single-axial flow focusing have indicated that the instability of the liquid cone upstream the orifice corresponds to the global instability; once the cone gets steadily formed, the breakup of interface into droplets corresponds to the local instability.[9,25] Gañán-Calvo et al. have performed a spatiotemporal instability analysis of liquid–gas jets in single-axial flow focusing, indicating that the absolute instability (AI) dominates the flow invariably, which verifies the experimental observations that only dripping mode of bubbling exists.[19] In the convective instability (CI) regime, the temporal instability analysis has been implemented to study the breakup behavior of coaxial liquid jets in flow focusing,[8,26] predicting the growth rate and corresponding wavelength of disturbances deposited on the jet interface. Herrada et al. have studied the CI/AI characteristics of the coaxial jets in CFF for the first time, by ignoring the outermost driving fluid and employing the uniform velocity profiles of the inner and outer jets, and the theoretical results are also compared with the experimental ones.[5] Despite the existing studies on the flow behaviors, a systematic study on the jetting and dripping modes in CFF is still desired, especially through the integration of experiments, numerical simulations, and theoretical analysis, for a better understanding of the underlying physical mechanisms of coaxial liquid interfaces into droplets in the CFF process.

In this work, the characteristics of jetting and dripping modes in CFF are presented in experiments and numerical simulations, and the transition between them is analyzed by scaling analysis. The spatiotemporal instability analysis is further performed by considering the real flows of triple-liquids and utilizing the basic velocity profiles

obtained from numerical simulations. An energy budget analysis is also implemented to access the dominating forces for the interfacial instability and mode transition in CFF. The theoretical results are further compared with the experimental ones. Finally, main conclusions are drawn.

II. METHODOLOGY

A. Experimental setup

The experimental setup for the CFF process is shown in Fig. 1(a), in which two immiscible liquids of flow rate Q_1 for the core phase and Q_2 for the shell phase are supplied out of the coaxial needle, and get focused at the orifice by the driving liquid with flow rate Q_3, forming the cone-jet configuration. The coaxial needle which consists of an inner and an outer stainless steel needle is manufactured by a laser beam welding process,[6] and the tips of two stainless needles are flattened and their edges are rounded to weaken the disturbances brought by the driving flow. The geometric parameters are kept constant and given as follows. The inner and outer diameters of the inner needle are $D_{1i} = 400\,\mu m$ and $D_{1o} = 625\,\mu m$, and the inner and outer diameters of the outer needle are $D_{2i} = 1050\,\mu m$ and $D_{2o} = 1490\,\mu m$, respectively. The orifice diameter D is $820\,\mu m$ and the thickness of the orifice is $T = 1100\,\mu m$. The distance between the outer needle exit and the orifice is $H = 660\,\mu m$, and the distance between the inner and the outer needles is $h = 100\,\mu m$, respectively.

We choose distilled water as the core and driving liquids, and silicone oil as the shell liquid. The density and viscosity of distilled water are $\rho_1 = 996\,kg\,m^{-3}$ and $\mu_1 = 0.001\,Pa\,s$, and the density and viscosity of the silicone oil are $\rho_2 = 965\,kg\,m^{-3}$ and $\mu_2 = 0.02\,Pa\,s$, respectively. The oil–water interfacial tension coefficient is $\gamma = 32.8\,mN\,m^{-1}$. A volume fraction of 3% blue ink is added in the core phase in order to visualize the inner liquid clearly. Quantitative measurement on physical properties indicates that little change of interfacial tension and viscosity occurs for the core liquid (less than 5%). The flow rates of core, shell, and driving liquids are controlled by the syringe pumps (WK-101P, Nanjing Anerke Electronics Technology, China), and the flow behavior is recorded by a CCD camera (DFK23G274, Allied vision

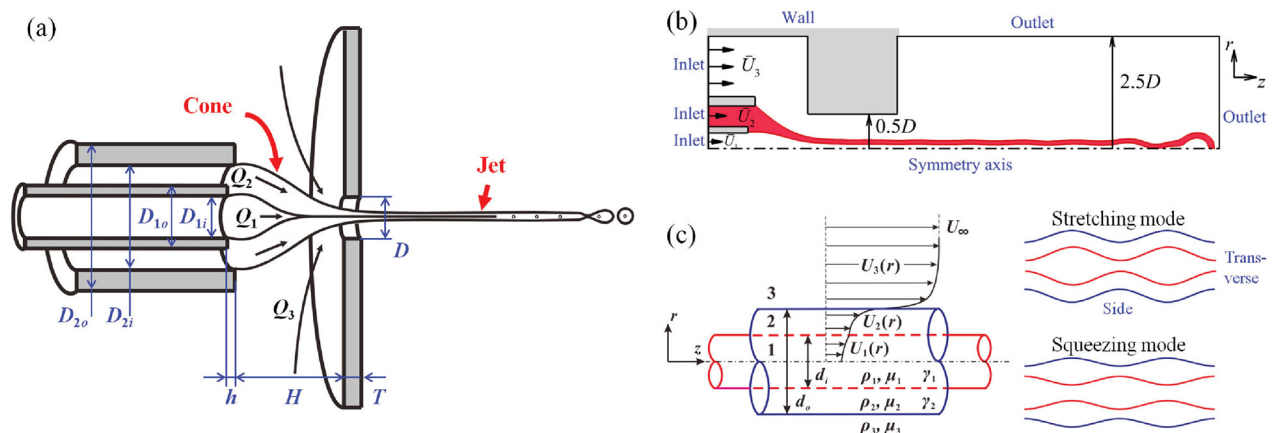

FIG. 1. (a) Sketch of the CFF process showing the formation of steady coaxial cone-jet configuration. (b) Computational domain of numerical simulations, where $\bar{U}_1$, $\bar{U}_2$, and $\bar{U}_3$ stand for the inlet flow velocities of core, shell, and driving phases, respectively. (c) Theoretical model of the coaxial liquid jets and sketch of two disturbance modes for the interfaces.

technologies, China) equipped with a microscopic lens (Leica Z16 APO, Germany) under the back-lighting illumination from a strobe flashlight (PS-01B, Hangzhou light tong boke automatic instrument, China, flashing frequency 3 kHz).

B. Direct numerical simulations

In numerical simulations, we solve the Navier–Stokes equations combined with a diffuse interface method. Figure 1(b) shows the schematic map of the CFF model, which consists of the coaxial needle, the sealed chamber, the focusing orifice, and the connective collector. A computational domain of $2.5D \times 12.5D$ is used for the axisymmetrical simulation, and the domain is sufficiently long for the liquid jet to evolve until breakup. The interface is represented by the liquid volume fraction, C, and its time evolution is governed by the Cahn–Hilliard equation[27]

$$\frac{\partial C}{\partial t} + \nabla \cdot (\mathbf{u}C) = \frac{1}{Pe}\nabla^2 \psi, \qquad (1)$$

where $\mathbf{u}$ denotes the flow velocity, and the chemical potential ψ is defined as

$$\psi = C^3 - 1.5C^2 + 0.5C - Cn^2\nabla^2 C, \qquad (2)$$

where the Cahn number Cn is a dimensionless thickness of the diffuse interface. In this work, the liquid interface is represented by the $C = 0.5$ contour, Cn is set to $0.5\Delta x$ where Δx is the mesh size, and the Peclet number is chosen as $Pe = 1/Cn$ following our previous work.[7] All the computational cases are performed on $\Delta x = 0.002D$, which is sufficient to resolve the flows for the core and shell phases.

In the numerical simulations, the motion of liquids is governed by the dimensionless Navier–Stokes equations

$$\rho\left(\frac{\partial \mathbf{u}}{\partial t} + \mathbf{u} \cdot \nabla \mathbf{u}\right) = -\nabla p + \frac{1}{Re}\nabla \cdot [\mu(\nabla \mathbf{u} + \nabla \mathbf{u}^T)] + \frac{\mathbf{f}_s}{We}, \quad (3)$$

$$\nabla \cdot \mathbf{u} = 0, \qquad (4)$$

where $\mathbf{f}_s = 6\sqrt{2}\Psi\nabla C/Cn$ denotes the interfacial tension force. It should be emphasized that in numerical methods, the interfacial tension force is directly added into the Navier–Stokes equations as a body force.[28] $\rho = C + r_\rho(1 - C)$ and $\mu = C + r_\mu(1 - C)$ denote the dimensionless averaged density and viscosity, and $r_\rho = \rho_1/\rho_2$ and $r_\mu = \mu_1/\mu_2$ are the density and viscosity ratios between the core and shell liquids, respectively. In simulations, D_{2i} and the average velocity of shell liquid, which is calculated by $\bar{U}_2 = 4Q_2/\pi \cdot (D_{2i}^2 - D_{1o}^2)$, are selected as the characteristic length and velocity, and accordingly, the Weber number and the Reynolds number are defined as $We_2 = \rho_2\bar{U}_2^2 D_{2i}/\gamma$ and $Re_2 = \rho_2\bar{U}_2 D_{2i}/\mu_2$, respectively. We also refer to the Weber number which represents the dimensionless flow rate of core liquid $We_1 = \rho_1\bar{U}_1^2 D_{1i}/\gamma$, the flow rate ratio between the driving and shell fluids $r_Q (= Q_3/Q_2)$, and the Ohnesorge number $Oh_2 = \mu_2/\sqrt{\rho_2\gamma D_{2i}}$. According to the experimental parameters, $Oh_2 = 0.104$, $r_\rho = 1.031$ and $r_\mu = 0.05$, and the values of We_1, We_2, r_Q change with the flow rates of the core, shell, and driving liquids.

Figure 1(b) also shows the boundary conditions of the computational domain. The boundary conditions for the velocity are implemented as follows: $v = 0, \partial u/\partial r = 0$ at $r = 0$, where u and v are the r and z components of the flow velocity, respectively; no-slip condition at the solid wall; $u = u_{in}$ and $v = 0$ at the inlet, where u_{in} is a

prescribed value which corresponds to the liquid flow rate; $\partial u/\partial z = \partial v/\partial z = 0$ at the outlet. The numerical method has been successfully validated in previous studies of single-axial flow focusing[18,29,30] and CFF[7] problem. The numerical results are also compared with the experiments at different flow modes in this work as indicated in Fig. 2.

C. Linear spatiotemporal instability analysis

To study the mechanism for the transition of flow modes in CFF, we also consider the linear spatiotemporal instability of the coaxial jets (inner jet: diameter d_i, density ρ_1, dynamic viscosity μ_1, average velocity U_1; outer jet: diameter d_o, density ρ_2, dynamic viscosity μ_2, average velocity U_2) in the cylindrical coordinate (z, r). The coaxial jets move in an infinite annular driving stream (with density ρ_3 and dynamic viscosity μ_3), as sketched in Fig. 1(c). The interfacial tensions between inner/outer jets and outer jet/driving stream are denoted by γ_1 and γ_2, respectively. The outer jet radius $d_o/2$ and its average velocity U_2 are chosen as the characteristic length and velocity, and the dimensionless parameters for the coaxial jets are the Weber number $We_c = \rho_2 U_2^2 d_o/2\gamma_2$, the Reynolds number $Re_c = \rho_2 U_2 d_o/2\mu_2$, the diameter ratio between the inner and outer jets $\kappa = d_i/d_o$, the density ratio $S = \rho_1/\rho_2, Q = \rho_3/\rho_2$, the viscosity ratio $N = \mu_1/\mu_2$, $M = \mu_3/\mu_2$, and the interfacial tension ratio $\tau = \gamma_1/\gamma_2$. For the liquids considered in our experiments and numerical simulations, $S = Q = 1.031$, $M = N = 0.05$, and $\tau = 1$, and We_c, Re_c and κ vary with the flow rates.

The normal mode method is implemented in the instability analysis of the coaxial liquid jets,[8] in which all the flow variables are split into a basic quantity and a small perturbation with the form $e^{i(\alpha z - \beta t)}$ in the cylindrical coordinates (z, r),

$$\boldsymbol{u}_i = U_i(r)\boldsymbol{e}_z + (\hat{v}_i(r), \hat{u}_i(r))e^{i(\alpha z - \beta t)},$$

$$p_i = P_i + \hat{p}_i(r)e^{i(\alpha z - \beta t)}, r_j = \kappa^{\delta_{j1}} + \eta_j e^{i(\alpha z - \beta t)}, \qquad (5)$$

where δ is the Kronecker function, $\boldsymbol{e}_z$ is the unit vector in the z-direction, $\alpha = \alpha_r + i\alpha_i$ is the complex axial wavenumber, $\beta = \beta_r + i\beta_i$ is the complex frequency, $\hat{v}_i(r), \hat{u}_i(r)$ are the amplitude of velocity perturbation in the r and z directions, respectively; $\hat{p}_i(r)$ is the amplitude of pressure perturbations, and $\eta_j (j = 1, 2)$ are the perturbation amplitudes on the inner $(j = 1)$ and the outer $(j = 2)$ interfaces.

Substituting these variables into Navier–Stokes equations and neglecting the high-order terms, we can get the linearized governing equations

$$\frac{d\hat{v}_i}{dr} + \frac{\hat{v}_i}{r} + i\alpha\hat{u}_i = 0, \qquad (6)$$

$$\frac{1}{Re_i}\left[\frac{d^2\hat{v}_i}{dr^2} + \frac{1}{r}\frac{d\hat{v}_i}{dr} - \left(\alpha^2 + \frac{1}{r^2} + i\alpha Re_i U_i\right)\hat{v}_i\right]$$

$$- \left(\frac{1}{S}\right)^{\delta_{i1}}\left(\frac{1}{Q}\right)^{\delta_{i3}}\frac{d\hat{p}_i}{dr} + i\beta\hat{v}_i = 0, \qquad (7)$$

$$\frac{1}{Re_i}\left[\frac{d^2\hat{u}_i}{dr^2} + \frac{1}{r}\frac{d\hat{u}_i}{dr} - (\alpha^2 + i\alpha Re_i U_i)\hat{u}_i\right]$$

$$- \frac{dU_i}{dr}\hat{v}_i - \left(\frac{1}{S}\right)^{\delta_{i1}}\left(\frac{1}{Q}\right)^{\delta_{i3}}i\alpha\hat{p}_i + i\beta\hat{u}_i = 0, \qquad (8)$$

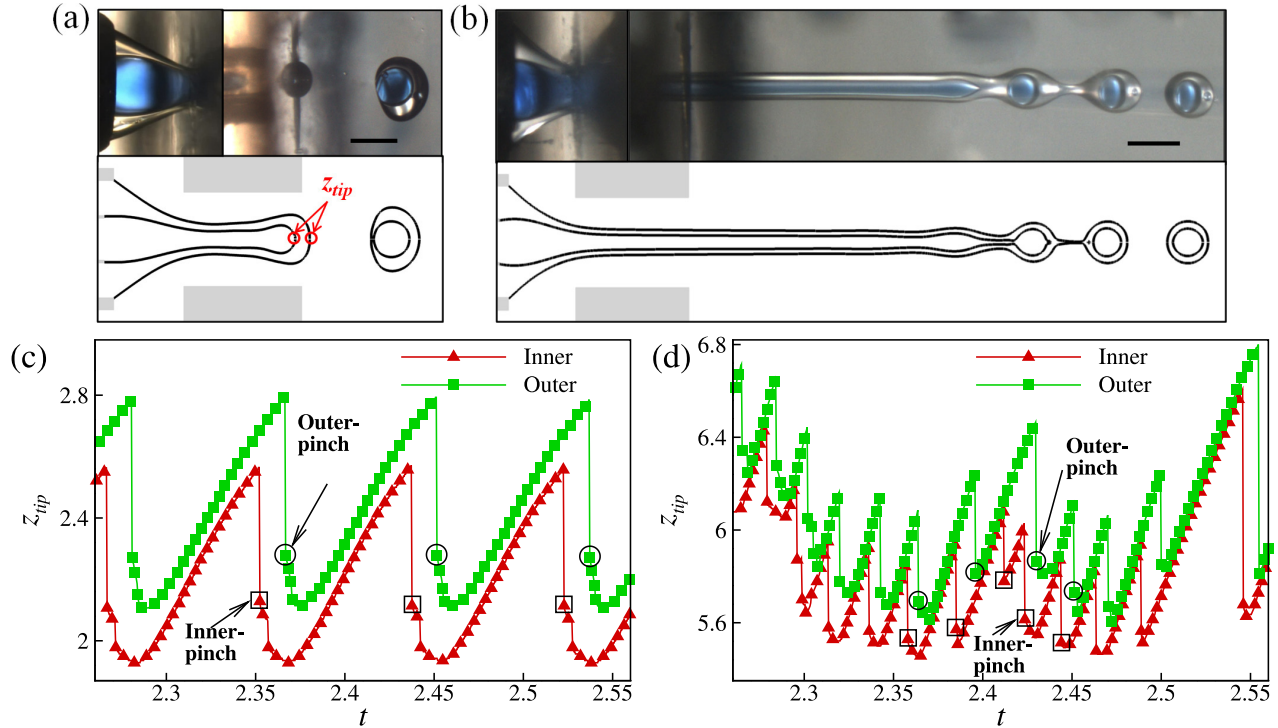where the Reynolds number $Re_1 = Re_c \cdot S/N$, $Re_2 = Re_c$, $Re_3 = Re_c \cdot Q/M$.

FIG. 2. Evolutions and breakup modes of liquid interfaces under a stable cone in CFF. (a) Dripping mode at $Q_1 = 20$, $Q_2 = 80$, and $Q_3 = 1000$ ml h^{-1}, corresponding to $We_1 = We_2 = 0.025$ and $r_Q = 12.5$ in numerical simulations; (b) jetting mode at $Q_1 = 35$, $Q_2 = 65$ and $Q_3 = 1400$ ml h^{-1}, corresponding to $We_1 = 0.072$, $We_2 = 0.016$, and $r_Q = 21.5$. Scale bar: 500 μm. (c) and (d), evolutions on tip of the interfaces and pinch-off positions for the dripping and jetting mode corresponding to the cases in (a) and (b), respectively.

For the boundary conditions, the velocity and the pressure at the symmetry axis $r = 0$ satisfy the consistency conditions

$$\hat{v}_1 = \frac{d\hat{u}_1}{dr} = \frac{d\hat{p}_1}{dr} = 0. \tag{9}$$

At the interfaces $r_j = \kappa^{\delta_{j1}} + \eta_j e^{i(\alpha z - \beta t)} (j = 1, 2)$, the continuity of velocity, the kinematic boundary condition, and the force balance on the tangential and normal directions are satisfied,

$$\hat{v}_j = \hat{v}_{j+1}, \hat{u}_j + \frac{dU_j}{dr}\eta_j = \hat{u}_{j+1} + \frac{dU_{j+1}}{dr}\eta_j, \tag{10}$$

$$-i\beta\eta_j = \hat{v}_j - i\alpha U_{sj}\eta_j, \tag{11}$$

$$\hat{p}_{j+1} - \frac{2M^{\delta_{j2}}}{Re_c}\frac{d\hat{v}_{j+1}}{dr} - \hat{p}_j - \frac{2N^{\delta_{j1}}}{Re_c}\frac{d\hat{v}_j}{dr} = \frac{\tau^{\delta_{j1}}}{We_c}\left(\frac{1}{\kappa^{2\delta_{j1}}} - \alpha^2\right)\eta_j, \tag{12}$$

$$N^{\delta_{j1}}\left(i\alpha\hat{v}_j + \frac{d\hat{u}_j}{dr} + \frac{d^2 U_j}{dr^2}\eta_j\right) = M^{\delta_{j2}}\left(i\alpha\hat{v}_{j+1} + \frac{d\hat{u}_{j+1}}{dr} + \frac{d^2 U_{j+1}}{dr^2}\eta_j\right). \tag{13}$$

The infinity boundary conditions at $r \to \infty$ are

$$\hat{v}_3 = \hat{u}_3 = \hat{p}_3 = 0. \tag{14}$$

It is notable that comparing with the temporal analysis of the coaxial jets,[8] in which the growth of interface disturbance ($\beta = \beta_r + i\beta_i$) is considered under a real wavenumber, the spatiotemporal analysis studies the growth of interface disturbances on a complex wavenumber region ($\alpha = \alpha_r + i\alpha_i$). The Chebyshev spectral collocation method[31] is utilized to solve Eqs. (6)–(14) numerically. A MATLAB code is developed to solve the dispersion relation of

$$D(\beta, \alpha; We, Re, \kappa, S, Q, M, N, \tau) = 0. \tag{15}$$

Generally, there are two growing modes of interface disturbances for the coaxial jets, as shown in Fig. 1(c): the stretching mode, where perturbations of double interfaces grow in phase, and the squeezing mode, where perturbations of double interfaces grow out of phase. Previous temporal instability analysis[8,26] has concluded that the stretching mode would always lead to a larger growth rate at wide ranges of wavenumber, suggesting the dominance of in-phase perturbation on the jet breakup. Numerical simulations have also shown that the growth of interface perturbations on the inner jet can give rise to capillary pressure between the inner and outer interfaces and cause the synchronized perturbations of the coaxial jets in CFF.[7] Accordingly, only the stretching mode is considered for the spatiotemporal instability analysis in this work.

D. Energy budget analysis

Energy budget is an elaborate method to access the mechanism of jet instability, in which a control volume with its length equals to the disturbance wavelength is considered.[31–33] Through forming a dot

product of momentum equations with dimensionless disturbance velocity $\tilde{\boldsymbol{u}}_i$, integrating over the control volume V and a period $T = 2\pi/\beta_r$, and averaging over one wavelength λ and period T, one can obtain the equation describing the development of disturbance kinetic energy. Using the continuity equation to simplify it and the Gauss theorem to transfer the volume integrals to surface integrals, we can derive the energy equation,

$$
\frac{1}{T\lambda}\int_0^T \int_V \left(\frac{\partial}{\partial t} + \boldsymbol{U}_i \cdot \nabla\right) e\,\mathrm{d}V\mathrm{d}t
$$
$$
= -\frac{1}{T\lambda}\int_0^T\int_V \tilde{\boldsymbol{u}}_i \cdot [\tilde{\boldsymbol{u}}_i \cdot \nabla \boldsymbol{U}_i]\mathrm{d}V\mathrm{d}t - \frac{1}{T\lambda}\int_0^T\int_A p_i\tilde{\boldsymbol{u}}_i \cdot \boldsymbol{n}_i\mathrm{d}A\mathrm{d}t
$$
$$
+ \frac{1}{T\lambda\mathrm{Re}_i}\int_0^T\int_A (\tilde{\boldsymbol{u}}_i \cdot \boldsymbol{\tau}_i) \cdot \boldsymbol{n}_i\mathrm{d}A\mathrm{d}t - \frac{1}{2T\lambda\mathrm{Re}_i}\int_0^T\int_V \boldsymbol{\tau}_i \cdot \boldsymbol{\tau}_i\mathrm{d}V\mathrm{d}t,
$$
(16)

where the subscript $i = 1, 2$ represents the inner and outer liquids, $e = \tilde{\boldsymbol{u}}_i \cdot \tilde{\boldsymbol{u}}_i/2$ is the disturbance kinetic energy, and A is the surface of the control volume, respectively. The term on the left-hand side represents the rate of change of the disturbance kinetic energy. As for the terms on the right-hand side, the first term gives the work done by energy transfer between the basic flow and the disturbance, the second and third parts represent the work done by the pressure and the viscous stress of the fluid, and the fourth term denotes the viscous dissipation. After employing the dynamic boundary conditions to transform the second and third terms on the right-hand side in order to better explain the effect of interface motion, we can derive the energy budget as

$$
\begin{aligned}
KE_1 &= REY_1 + PRL_{1s} + NVL_{1s} + SUT_1 + PRL_{1r} + SHL_{1r} \\
&\quad + NVL_{1r} + SHB_1 + SHL_{1s} + DIS_1, \\
KE_2 &= REY_2 + PRL_{2s} + NVL_{2s} + SUT_2 + PRL_{2r} + SHL_{2r} \\
&\quad + NVL_{2r} + SHB_2 + SHL_{2s} + DIS_2.
\end{aligned}
$$
(17)

The detailed formula of each term can be found in the Appendix. The subscripts r and s stand for the transverse and side surface integrals of the control volume [see the sketch in Fig. 1(c)], respectively. KE_1 and KE_2 stand for the time rate of the kinetic energy of inner fluid and outer fluid; REY_1 and REY_2 denote the energy exchange between basic flow and disturbance velocities through the Reynolds stress of inner fluid and outer fluid; SUT_1 and SUT_2 are the rates of work done by the inner and outer interfacial tensions; SHB_1 and SHB_2 represent the rates of work done by the distortion of basic flow associated with the inner and outer surface displacements; DIS_1 and DIS_2 represent the rate of work contributed by the viscous dissipation. PRL_{1r} and PRL_{1s} are the rates of work done by the pressure fluctuation on the transverse and side parts of the inner fluid control volume, and so as to the PRL_{2r} and PRL_{2s}, which correspond to the outer fluid control volume. SHL_{1r} and SHL_{1s} stand for the work done by normal components of viscous stress at transverse and side sections of inner fluid, while SHL_{2r} and SHL_{2s} show them of outer fluid. NVL_{1r} and NVL_{1s} stand for the rates of work done by the tangential components of viscous stress at transverse and side sections of inner fluid, and so as to the NVL_{2r} and NVL_{2s}, which react to the outer fluid control volume. Because of the independence of each integrals, we can compare the KE_1 and KE_2 with the sum of all terms on the right-hand side to

guarantee the calculation accuracy. To access the mechanism for the instability of the coaxial jet, we can normalize these terms in Eq. (17) by the kinetic energy of the entire system (i. e., $KE = KE_1 + KE_2$) and evaluate the proportion of each term on the total kinetic energy. It is notable that a positive proportion of a certain term suggests that the corresponding force can promote the instability of the coaxial jets, while a negative proportion of a certain term means that the corresponding force would suppress the coaxial jet instability.

III. RESULTS AND DISCUSSION
A. Jetting and dripping modes

In CFF process, a coaxial cone would first form between the capillary tube and the orifice, then the coaxial interfaces are stretched at the orifice and finally break up to compound droplets downstream. Our previous studies on single-axial flow focusing have shown that the liquid cone may present either the temporally stable or unstable vibrating behaviors as the flow rates of driving or driven liquids to vary.[30,34] The presence of an unstable cone would lead to the interface breakup and droplet generation at the orifice exit or inside the orifice, and the size of the droplets is comparable with the orifice diameter. On the contrary, abundant flow modes can be observed under a stable cone, in which the jetting and dripping modes are the most typical,[14] and the size and generation frequency of droplets can be manipulated under different modes. In this work, we mainly focus on the breakup modes of liquid interfaces in CFF under a stable coaxial cone and study the mode transition systematically.

The experiments in Fig. 2 show that the jetting and dripping modes exist in CFF, similar to the single-axial flow focusing. Figure 2(a) presents the typical morphology of dripping mode, in which the compound droplets are generated right at the exit of the orifice, in the presence of nearly synchronized breakup of the inner and outer interfaces. Figure 2(b) presents the typical morphology of the jetting mode with the breakup of two coaxial jets. The numerical results of dripping and jetting modes are also given in Fig. 2 (see the lower half) under the same flow parameters as those in experiments, and a good agreement between them is obtained. To show the droplet formation characteristics under different flow modes, we trace the temporal evolution of the positions of the liquid interface tip z_{tip} for the inner and outer interfaces [sketched in Fig. 2(a)] numerically, as shown in Figs. 2(c) and 2(d), respectively. It is notable that z_{tip} is defined as the length from the capillary tube mouth to the interface tip with a tracer located at the downstream end of the interfaces. When the interface breaks up to droplet at the pinch-off instant, z_{tip} drops sharply due to the formation of a new interface tip. Therefore, the pinch-off positions can be obtained. For the dripping mode shown in Fig. 2(c), the evolution of both the inner and outer interfaces is temporally periodic with a certain pinch-off position, leading to compound droplets with uniform size. For the jetting mode [see Fig. 2(d)], the interface evolution usually presents the aperiodic behavior due to the random disturbances of the coaxial jets,[24] which would lead to multiple pinch-off positions and compound droplets with non-uniform size. Moreover, as the larger value of r_Q for the jetting mode in Fig. 2(b) leads to a faster flow velocities for the driving liquid comparing with the dripping mode in Fig. 2(a), the frequency for the droplet generation is much larger in the jetting mode.

Figure 3 illustrates the transition from dripping mode to jetting mode as the flow rates of the core, shell, and driving liquids (i.e., Q_1,
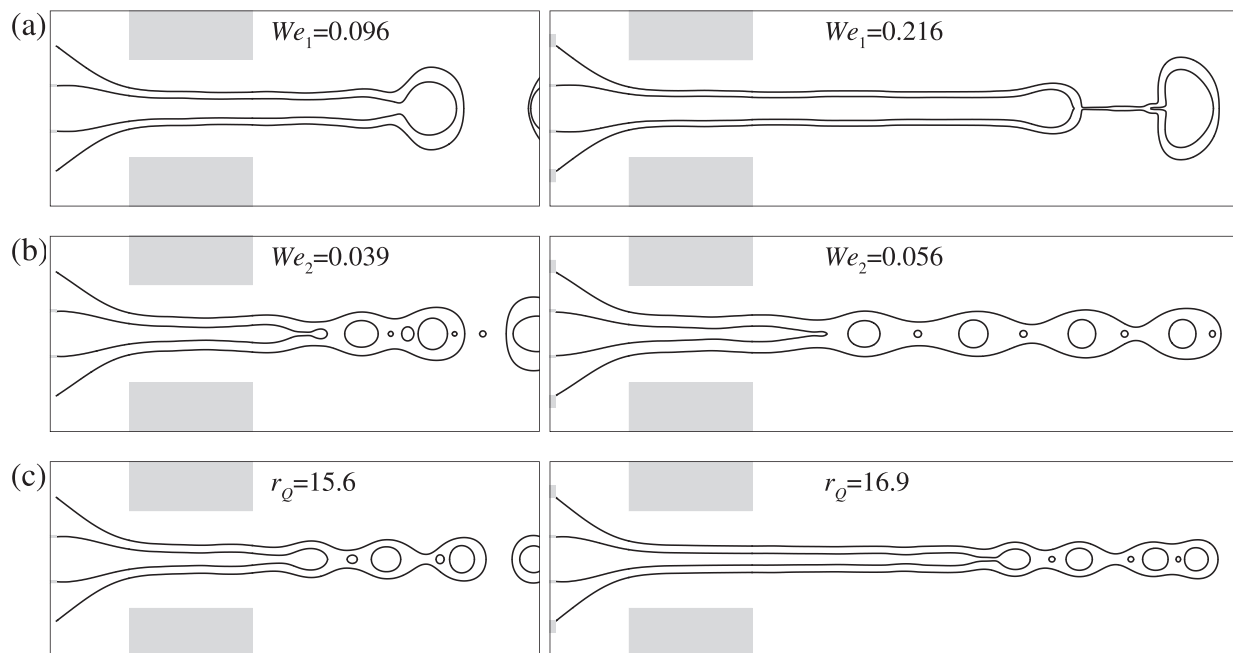
FIG. 3. Interface profiles as liquid flow rates gradually increase comparing with the reference case in Fig. 2(a) where $We_1 = We_2 = 0.025$ and $r_Q = 12.5$ ($Q_1 = 20$, $Q_2 = 80$, and $Q_3 = 1000$ ml h^{-1}). (a) We_1 singly increases, corresponding to the increase in Q_1 to 40 and 60 ml h^{-1}; (b) We_2 increases at certain $We_2 \cdot r_Q^2 = 3.9$, corresponding to the increase in Q_2 to 100 and 120 ml h^{-1}; (c) r_Q singly increases, corresponding to the increase in Q_3 to 1250 and 1350 ml h^{-1}.

Q_2, and Q_3, respectively) gradually increase in comparison with the reference case in Fig. 2(a). According to our definition of the dimensionless parameters, it is noteworthy that the singe variation of Q_1 [see Fig. 3(a)] corresponds to the change of We_1 at certain values of We_2 and r_Q, the singe variation of Q_2 [see Fig. 3(b)] corresponds to the change of We_2 at certain values of We_1 and $We_2 \cdot r_Q^2$, and the singe variation of Q_3 [see Fig. 3(c)] corresponds to the change of r_Q at certain values of We_1 and We_2, respectively. Comparing with the interface profiles of dripping mode in Fig. 2(a), it is clear that the increase in either flow rate can lead to the formation of coaxial liquid jets at the tip of the cone, promoting the transition from dripping mode to jetting mode. Once the coaxial jets are established, the jet breakup length would gradually increase as the liquid flow rates increase. Moreover, the coupling manners on the breakup of inner and outer jets are significantly affected by the flow rates. The coupling of interface breakup and its influence on the compound droplets generation have been studied in our previous work.[7]

To study the effect of liquid flow rates on modes transition systematically, the phase diagram of jetting and dripping modes is shown in Fig. 4. Figure 4(a) considers the jetting/dripping transition boundaries on $We_2 - r_Q$ plane at certain $We_1 = 0.025$, which correspond to the situations of changing Q_2 and Q_3 under a certain Q_1. Numerical results (solid lines) and two groups of experimental boundaries (symbols) are presented simultaneously. In experiments, one group of boundary ($\triangle$) is obtained by increasing r_Q from initial dripping mode, and the other group ($\bigcirc$) is obtained by decreasing r_Q from jetting mode. Error bars are given along with the symbols. It can be seen that the hysteresis effect on modes transition exists in experiments. In

single-axial flow focusing, the degree of hysteresis is considered to be closely related to the liquid viscosity and geometric parameters.[15] It is notable that as r_Q decreases to very low value, the stable coaxial cone cannot be maintained, which is shown by the gray zone in Fig. 4(a). Figure 4(b) further presents the effect of We_1 (corresponding to Q_1) on the jetting/dripping boundary through numerical simulations. Four values of We_1, including the single shell jet case where $We_1 = 0$, are considered and the relevant modes transition boundaries are plotted. It is clear that when We_1 is unequal to zero, the boundary would shift down as We_1 increases. Combining the results in Figs. 3 and 4, it can be concluded that an individual decrease in either We_1, We_2, or r_Q would all promote the transition from jetting to dripping modes.

In order to study the inducing factor for jetting/dripping transition, we present two special cases in Fig. 4(b), where $We_1 = 0$ or 0.025 at a certain $We_2 = 0.01$ and $r_Q = 24$, which correspond to the dimensional situation of $Q_1 = 0$ or 20 ml h^{-1} at fixed $Q_2 = 50$ and $Q_3 = 1200$ ml h^{-1}. When We_1 (Q_1) is equal to zero, the coaxial jets degenerates to a single outer jet. However, when $We_1 = 0.025$, the addition of inner interface would lead to the dripping mode of double interfaces, which means that the dripping behavior of inner interface destabilizes the outer jet right at the orifice and causes the synchronous dripping behavior of the outer interface. Actually, we have given the jetting/dripping transition boundary for a single jet (i.e., $We_1 = 0$) on $We_2 - r_Q$ plane in Fig. 4(b), which indicates that the transition boundary for a single jet would shift down comparing with that for a coaxial jet. It clearly indicates a dominant effect of inner interface on the occurrence of dripping mode. For example, at the space where r_Q is slightly over the boundary of the single jet case, the individual outer
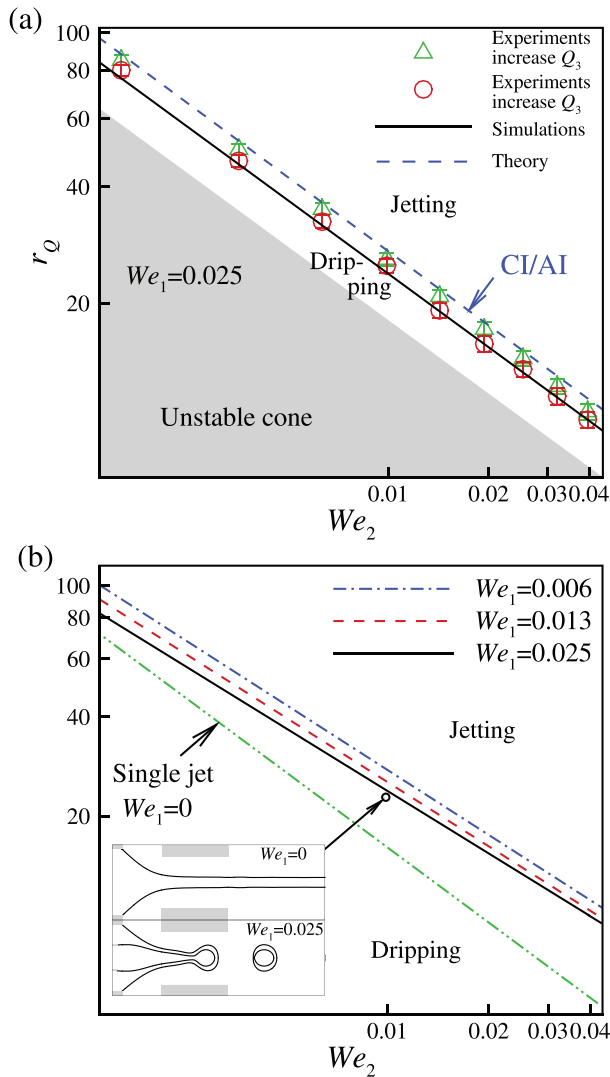
FIG. 4. (a) Transition boundaries of jetting/dripping mode on $We_2 - r_Q$ plane at certain $We_1 = 0.025$. Numerical boundary (solid line) is compared with two groups of experimental boundary obtained through either increasing or decreasing r_Q ($\triangle$, $\bigcirc$). The spatiotemporal convective/absolute instability (CI/AI) boundary is also given (dashed lines). (b) Numerical boundaries at different We_1 on $We_2 - r_Q$ plane, where boundaries of $We_1 = 0$ (dashed–dotted–dotted line), $We_1 = 0.006$ (dashed–dotted line), 0.013 (dashed line) and 0.025 (solid line) are depicted. The subgraph shows the flow patterns when $We_1 = 0$ or 0.025 at a certain $We_2 = 0.01$ and $r_Q = 24$.

interface can present the jetting mode. However, the coaxial interface would still present the dripping mode, which is induced by the dripping behavior of inner interface.

B. Scaling analysis for mode transition

The behaviors of jetting and dripping are physically considered to be dominated by force balance at the local position where a thin jet or a small droplet can be formed. Previous investigations on co-flowing microcapillary system[35] have suggested that if the inertia or

shear stress dominates the interfacial tension at the exit of capillary tube, a thread would emit from the capillary tube, presenting the jetting mode; otherwise, droplets would pinch off at the capillary tube, presenting the dripping mode. In the flow focusing process, however, the jet diameter is generally not at the same scale with the capillary tube diameter due to the existence of the cone. Therefore, it would be appropriate to consider the force balance at the local jet position rather than at the capillary tube exit.[29] In the CFF process, the breakup of inner interface dominates the mode transition, and therefore, it is reasonable to consider the force balance of local inner jet. The characteristic parameters of inner jet are

$$We_i = \frac{\rho_1 U_1^2 d_i}{\gamma}, \quad Ca_o = \frac{\mu_2 U_2}{\gamma}, \quad (18)$$

where d_i is the inner jet diameter, and U_1 and U_2 denote the average velocities of inner and outer jets, respectively. Physically, We_i and Ca_o reflect the competitions of inertia and viscous shear stress with the interfacial tension at the inner jet, respectively.

In experiments, the diameter of inner jet is difficult to measure directly because of the light refraction caused by the cylindrical outer jet. Here we perform the numerical simulations to provide an accurate measurement on the jet diameters and velocities. The values of We_1, We_2, or r_Q are changed separately by keeping the rest parameters constant in numerical simulations, and the jetting/dripping boundaries are identified. The corresponding values of We_i and Ca_o are indicated in Fig. 5(a), showing the transition from initial jetting regime either by singly decreasing r_Q ($\triangle$, $\diamond$, and $\circ$), We_1 (■), or We_2 (▼). The values of U_1, U_2, and d_i are measured at the orifice exit. It can be seen that as r_Q, We_1, or We_2 gradually decreases, the values of We_i and Ca_o decrease simultaneously (the change directions of We_i and Ca_o are shown by the gray arrow), suggesting a more important role played by the interfacial tension and weakening roles of inertia force and shear stress. When the liquid jet gives way to droplets at the orifice exit (i.e., in the dripping mode), the value of d_i cannot be obtained; thus for each group of case, the symbols at smallest We_i and Ca_o are approximately considered as the critical values of jetting/dripping transition. It is clearly seen that in all cases the jetting finally gives way to dripping close to $We_i + Ca_o = 1$ (i.e., the dashed line), suggesting that the transition is dominated by the competition of inertia force and shear stress with interfacial tension at the inner jet.

Figure 5(a) shows that the critical We_i ranges 0.6–0.85 and the critical Ca_o ranges 0.25–0.4, which reflects that the inertia force and the shear stress act cooperatively to maintain a stable jet. This is different from the single-axial flow focusing cases in which the inertia force can provide the main contribution for a stable jet.[29,36] The remarkable role played by the shear stress in CFF can be attributed to the high viscosity of the outer liquid jet. An intuitional understanding of the effect of high outer jet viscosity is that it would produce large viscous shear stress on the inner jet, leading to a decrease in inertia force needed to maintain the jet. Through numerical simulations, Fig. 5(b) further indicates the influence of outer jet viscosity on the critical values of We_i and Ca_o. We compare three groups of cases where $Oh_2 = 0.026$, $r_\mu = 0.2$; $Oh_2 = 0.104$, $r_\mu = 0.05$; and $Oh_2 = 0.26$, $r_\mu = 0.02$ at certain $We_1 = We_2 = 0.025$, corresponding to single change of the outer jet dynamic viscosity of 0.005, 0.02, and 0.05 Pa s, respectively. Through decreasing r_Q from the jetting region, we can obtain the critical We_i and Ca_o in Fig. 5(b). It can be seen that as Oh increases (i.e., the outer
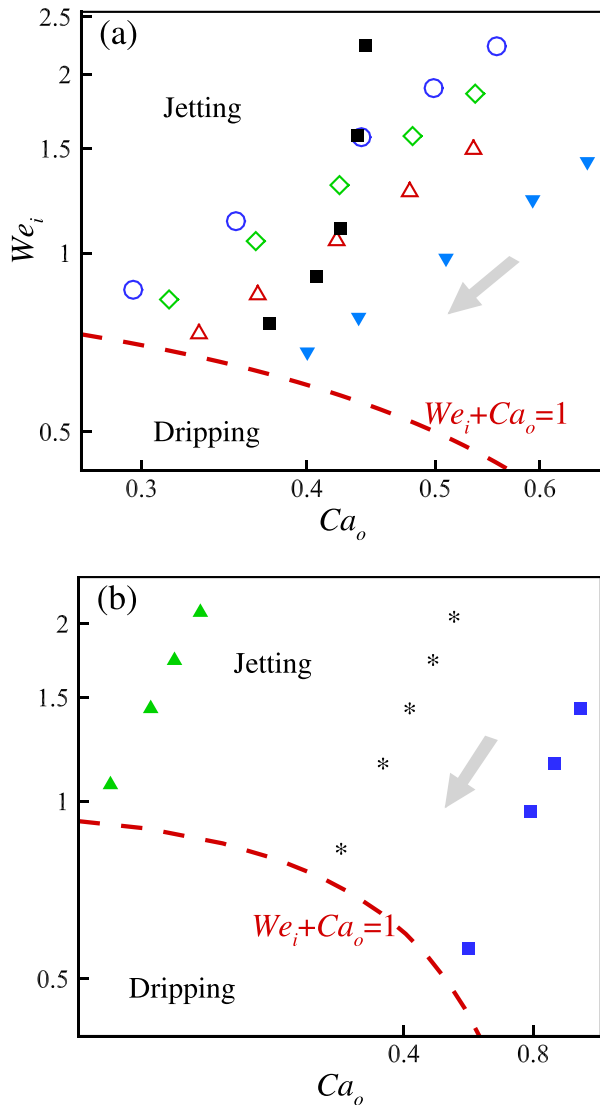
FIG. 5. Phase diagram of jetting and dripping on $We_i - Ca_o$ plane. (a) The jetting/dripping transition as r_Q, We_2 or We_1 varies individually. $\triangle$: $We_1 = 0.006$, $We_2 = 0.032$, r_Q decreases from 20 to 11.7; $\diamondsuit$: $We_1 = 0.013$, $We_2 = 0.028$, r_Q decreases from 21.2 to 12.4; $\circ$: $We_1 = 0.025$, $We_2 = 0.04$, r_Q decreases from 18 to 9.5. $\blacktriangledown$: $We_1 = 0.025$, $r_Q = 28$, We_2 decreases from 0.019 to 0.009. $\blacksquare$: $We_2 = 0.014$, $r_Q = 23.3$, We_1 decreases from 0.025 to 0.003. (b) The jetting/dripping transition as r_Q decreases at certain $We_1 = We_2 = 0.025$ under different dynamic viscosity of the shell liquid. $\blacktriangle$: $Oh_2 = 0.026$, $r_\mu = 0.2$; $*$: $Oh_2 = 0.104$, $r_\mu = 0.05$; $\blacksquare$: $Oh_2 = 0.26$, $r_\mu = 0.02$. The gray arrow denotes the change direction of We_i and Ca_o as the parameters We_1, We_2, or r_Q decrease. In all cases, the transition from jetting to dripping occurs close to $We_i + Ca_o = 1$ (dashed line).

jet viscosity increases), the critical Ca_o increases and the corresponding We_i decreases, suggesting a more significant role played by the viscous shear stress and a weakening role played by the inertia force. From the order of critical We_i and Ca_o, it can be seen that for $Oh_2 = 0.026$, the inner jet is maintained mainly by the inertia force as $We_i \sim O(1)$, $Ca_o \sim O(10^{-2})$; while for $Oh_2 = 0.104$ and 0.26, the inner jet is maintained corporately by the inertia force and the shear

stress as $We_i \sim O(10^{-1})$, $Ca_o \sim O(10^{-1})$. As a result, the transition boundary between jetting and dripping modes is close to $We_i + Ca_o = 1$ for each case.

We also deduce the relationship between We_i, Ca_o, and the flow parameters to provide a straightforward prediction on mode transition. Previous studies have concluded that an approximately equal average velocity of inner and outer jets and the driving stream can be assumed due to the viscous diffusion,[7,15,37] which implies that

$$\frac{Q_1}{d_i^2} \approx \frac{Q_2}{d_o^2 - d_i^2} \approx \frac{Q_3}{D^2 - d_o^2}. \tag{19}$$

According to the definition of We_i and Ca_o in Eq. (18), we can obtain

$$We_i \approx \frac{16\rho_1}{\pi^2 \sigma D^3} Q_1^{\frac{1}{2}} Q_3^{\frac{3}{2}}, Ca_o \approx \frac{4\mu_2}{\pi \sigma D^2} Q_3. \tag{20}$$

The equations can also be rewritten in the dimensionless form

$$We_i \approx \Theta \cdot We_1^{\frac{1}{4}} We_2^{\frac{3}{4}} r_Q^{\frac{3}{2}}, Ca_o \approx \Omega \cdot We_2^{\frac{1}{2}} Oh_2 r_Q, \tag{21}$$

where $\Omega = (D_{2i}^2 - D_{1o}^2)/D^2$, $\Theta = r_\rho^{3/4}(D_{1i}/D_{2i})^{3/4}\Omega^{3/2}$. In our situations considered, the coefficients are $\Theta = 0.70$ and $\Omega = 1.31$, respectively. Equation (21) directly shows the effect of process parameters on the inertia and shear force of the jet. Moreover, as the jetting/dripping boundary can be approximated by the relationship $We_i + Ca_o = 1$, Eq. (21) also gives a guideline to predict the flow mode under given parameters.

C. Spatiotemporal instability and energy budget analysis

In linear spatiotemporal instability analysis, the evolution of small disturbances superposed on a basic flow state is solved through
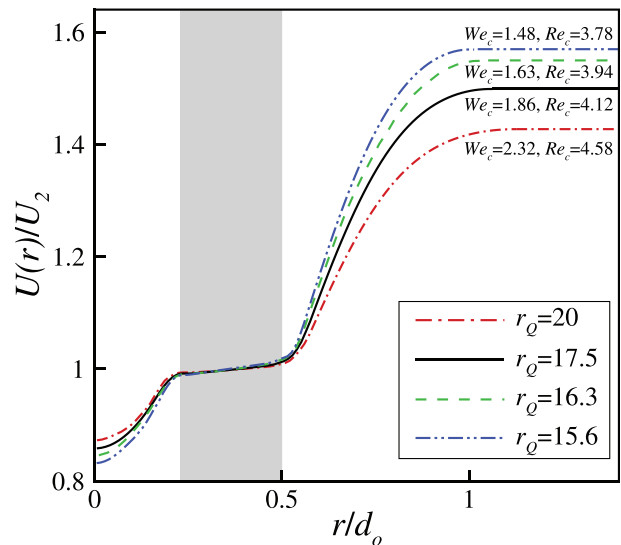

FIG. 6. Numerical velocity profiles of the coaxial jets measured at the exit of orifice, where $We_1 = We_2 = 0.025$ and $r_Q = 20, 17.5, 16.3$, and 15.6, respectively. The corresponding parameters of the coaxial jet: $\kappa = 0.46$, $S = Q = 1.031$, $M = N = 0.05$, $\tau = 1$, the basic velocity profiles and the values of We_c and Re_c vary with r_Q.

the normal mode method, the detail of which is shown in Sec. II C. For the coaxial jets, it is difficult to obtain the analytic solution of basic flows by directly solving the Navier–Stokes equations coupled with boundary conditions. Thus, approximate basic flows, such as the uniform velocity profile,[5,15] or the profile based on mathematical functions,[8,14] are widely used in the instability analysis. In this work, we utilize the numerical velocity profile measured at the exit of focusing orifice as the basic flow of the coaxial jets, considered to approximate the real flow field in experiments. As an example, Fig. 6 shows a group of velocity profiles as r_Q varies at certain $We_1 = We_2 = 0.025$ (corresponding to $Q_1 = 20$ and $Q_2 = 80$ ml h^{-1}). For simplification, we ignore the shear layer of the outmost boundary since it is considered to have little influence on the jet instability.[8,14] Therefore, the basic

velocity profiles would keep constant along the radial direction after reaching the maximum value. In this situation, $\kappa = 0.46$ can be obtained. The basic velocity profiles and the values of We_c and Re_c would vary significantly with r_Q changing, as indicated in Fig. 6.

The complex wavenumber $\alpha = \alpha_r + i\alpha_i$ and frequency $\beta = \beta_r + i\beta_i$ are assumed in the spatiotemporal analysis. We choose the reference parameters of the coaxial jets at $We_1 = We_2 = 0.025$ and $r_Q = 20$ (corresponding to $Q_1 = 20$, $Q_2 = 80$ and $Q_3 = 1600$ ml h^{-1}), and the relevant parameters of the coaxial jets are $We_c = 2.32$, $Re_c = 4.58$, $S = Q = 1.031$, $M = N = 0.05$, $\kappa = 0.46$, and $\tau = 1$. In order to distinguish the instability characteristics of the coaxial jet, the saddle point[14,38] and the cusp point method[39] are utilized. Figure 7(a) shows the corresponding iso-potential contours of the growth rate β_i on the
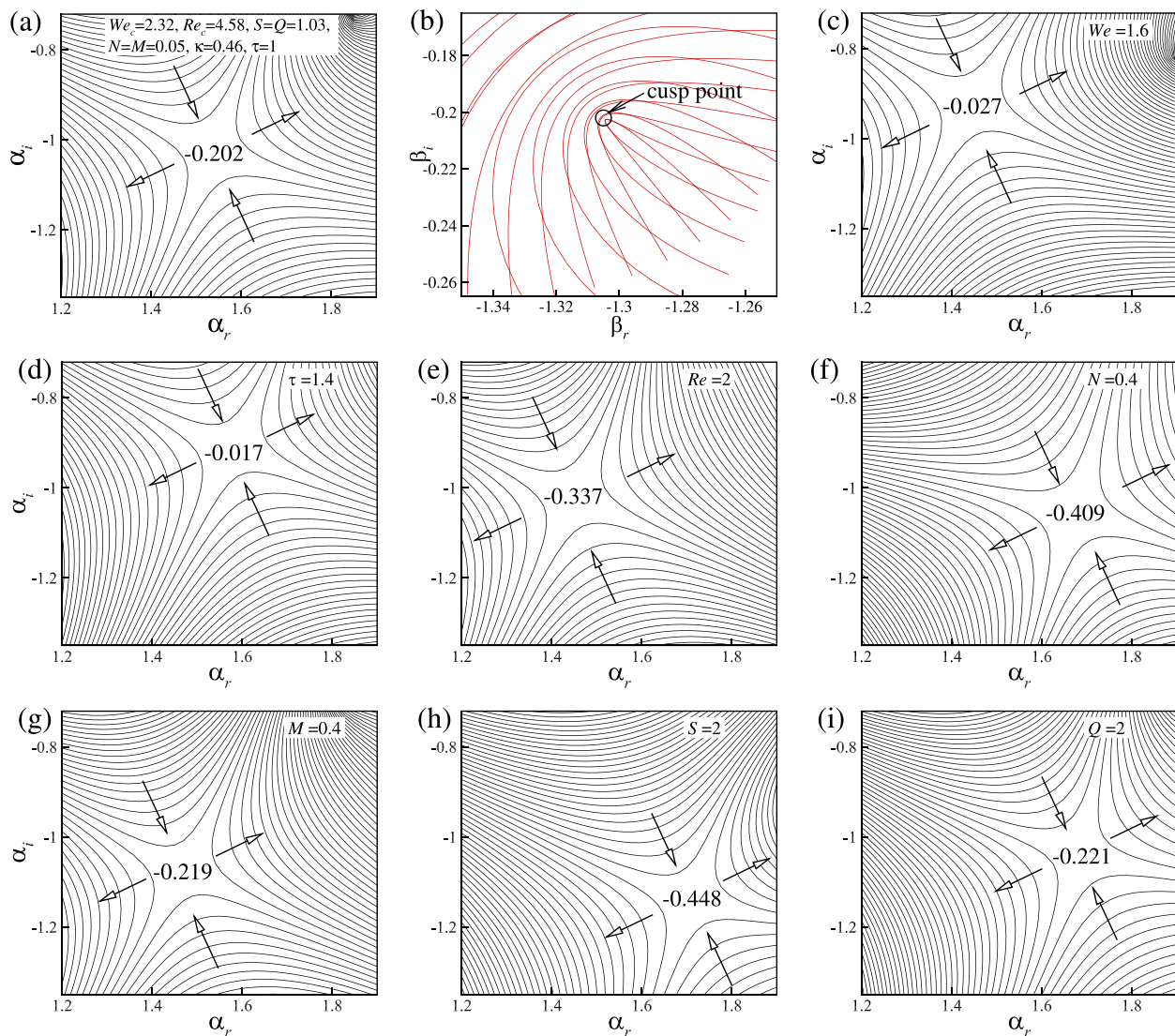

FIG. 7. (a) The isopotential line of β_i and the saddle point on the complex α plane at the reference state ($We_c = 2.32$, $Re_c = 4.58$, $S = Q = 1.03$, $N = M = 0.05$, $\kappa = 0.46$, $\tau = 1$). The arrows denote the direction where β_i decreases. (b) The isopotential line of α_i and the cusp point on the complex β plane at the reference state. (c)–(i) denote the isopotential line of β_i and the saddle point on α plane when We_c, τ, Re_c, N, M, S, and Q varies singly comparing with the reference state, respectively.

wavenumber $\alpha_r - \alpha_i$ plane, where the arrows denote the direction of β_i decreasing. As the branches where β_i decreases from positive values and β_i increases from negative values approach, a saddle point (or called pinching point) occurs. It has been known that if $\beta_i > 0$ at the saddle point, the coaxial jets behave at convective instability (CI), where the interface disturbance only grows downstream the flow; if $\beta_i < 0$, the coaxial jets behave at absolute instability (AI), where the interface disturbance grows both upstream and downstream the flow.[14] Physically, the CI corresponds to the jetting mode of coaxial interfaces, and AI corresponds to the dripping mode. For the reference case shown in Fig. 7(a), $\beta_i = -0.202$ at the saddle point, suggesting that the coaxial jets operate at CI and present the jetting mode, which is consistent with the numerical results. Figure 7(b) further shows the iso-potential contours of α_i on the complex $\beta_r - \beta_i$ plane, in which the cusp point can be identified.[39] It can be seen that the cusp point occurs below the real axis ($\beta_i = -0.202$), which is consistent with the result of saddle point.

Based on the reference case, we further investigate the effect of parameters including the interfacial tensions of inner and outer interfaces represented by We_c and τ, the dynamic viscosities of core, shell, and driving liquids represented by Re_c, M, and N, and the density ratios of core and driving liquids to shell phase (S and Q). For simplicity, only the saddle points are shown. Figures 7(b) and 7(c) show that a decrease in We_c or an increase in τ would enlarge the β_i at saddle point, suggesting that the increase in interfacial tensions would promote the AI and facilitate the dripping mode. Figures 7(d)–7(f) show that a decrease in Re_c or an increase in N and M would decrease the β_i at saddle point, suggesting that increasing the fluid viscosities can promote the CI as well as the jetting mode. The effects of liquid densities on the saddle points are shown in Figs. 7(g) and 7(h), indicating that an increase in S or Q would also promote the CI and the jetting mode as the β_i at saddle point gets smaller.

We compare the theoretical boundary of CI/AI with the flow modes boundary of jetting/dripping at certain $We_1 = 0.025$, which correspond to the cases considered in Fig. 4(a). As an example, for the case $We_2 = 0.025$, we can calculate the saddle point and cusp point based on the corresponding parameters and velocity profiles for the coaxial jets as r_Q gradually decreases to reach the modes transition boundary, as shown in Fig. 8. It can be seen that as r_Q gradually decreases [Figs. 8(a)–8(d)], the We_c and Re_c of the coaxial jets would decrease simultaneously. Meanwhile, the flow will gradually approach AI as the β_i at saddle point increases close to zero. The increase in β_i can also be seen clearly from the cusp points, which gradually approach the real axis on $\beta_r - \beta_i$ plane from Figs. 8(a)–8(d). As r_Q decreases to 15.1, as shown in Fig. 8(d), β_i reaches zero at the saddle point, suggesting the boundary of CI/AI. Thus, $r_Q = 15.1$ can be treated as the transition boundary between jetting and dripping modes for a certain $We_2 = 0.025$. Similarly, all the critical r_Q under different We_2 in Fig. 4(a) can be got based on the saddle point method. The theoretical jetting/dripping boundary is shown on phase diagram of Fig. 4(a) by the dashed line, which presents an acceptable agreement with the experimental and numerical results.

The energy budget analysis at the saddle and cusp points is further given in Fig. 9 to show the mechanism of the transition between CI and AI, which considers the variation of r_Q in the parameter region of CI for the cases in Fig. 8. All the terms in the right-hand side of Eq. (17) are normalized by the total kinetic energy KE ($= KE_1 + KE_2$) of the coaxial jets. It is noteworthy that as the terms REY_i, SHL_{ir}, SHL_{is}, NVL_{ir}, SHB_i ($i = 1$ and 2) and SUT_2, NVL_{2s}, and PRL_{2r} are found to be much smaller than KE with their proportion less than 5%, they are negligible in the energy budget and not shown in Fig. 9. For the other terms in Eq. (17), Fig. 9 shows that the terms SUT_1, PRL_{1r}, and PRL_{2s} are positive, suggesting that the interfacial tension of inner jet, the pressure fluctuation on the transverse parts of the inner jet, and the pressure fluctuation on the side parts of the outer jet can promote
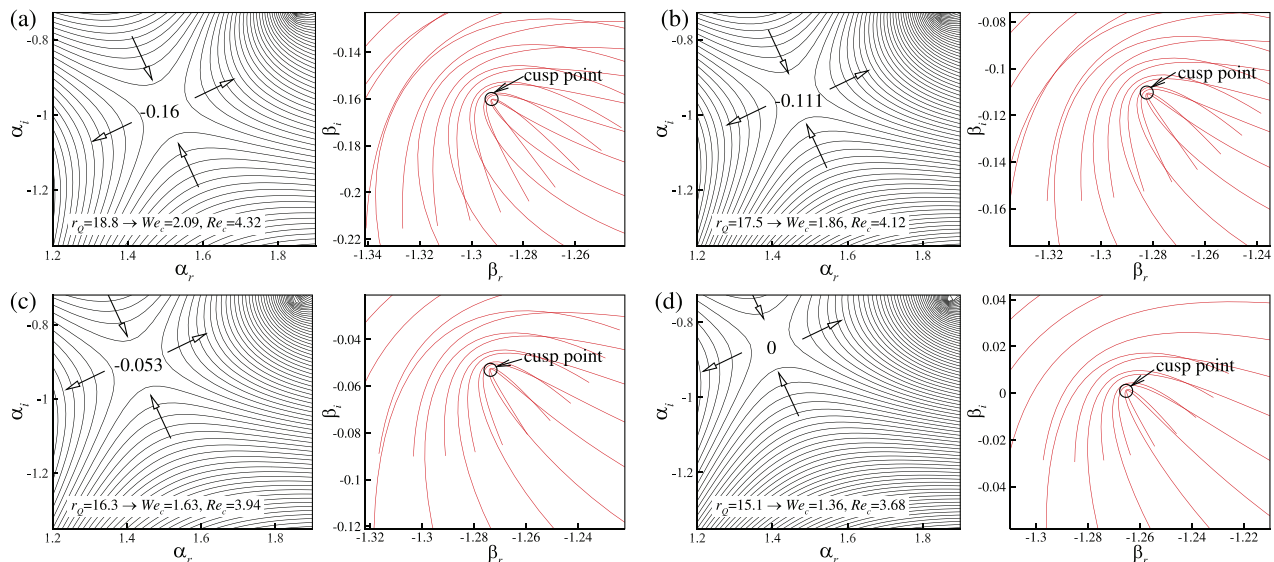

FIG. 8. The saddle points and cusp points at different r_Q under certain $We_1 = We_2 = 0.025$, which are obtained through the numerical velocity profile and the corresponding We_c and Re_c, respectively. (a) $r_Q = 18.8$. (b) $r_Q = 17.5$. (c) $r_Q = 16.3$. (d) $r_Q = 15.1$.
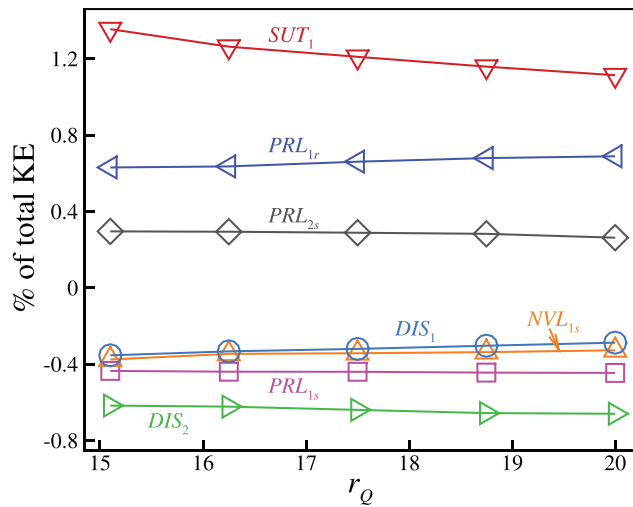
FIG. 9. Energy budget at the saddle point as r_Q varies, all the terms are normalized by the total kinetic energy $KE(= KE_1 + KE_2)$.

the instability of the coaxial jets; while the terms DIS_1, DIS_2, PRL_{1s}, and NVL_{1s} are negative, which suggests that the viscous dissipation of inner and outer jets, the pressure fluctuation and the normal viscous stress at side parts of the inner jet mainly restrain the coaxial jets instability. As the term SUT_1 would always have the largest positive value comparing with the other terms, the interfacial tension of inner jet will do a main contribution for the breakup of the coaxial jets. Moreover, when r_Q gradually decreases to reach the CI/AI boundary (i.e., $r_Q = 15.1$), the terms SUT_1 would increase monotonously, suggesting a more predominated role of interfacial tension of inner jet during the transition from jetting to dripping mode. The dominance of interfacial tension of inner jet on modes transition is in accordance with the scaling analysis in Sec. III B. Combing the spatiotemporal instability and energy budget analysis with the experimental and numerical results in Secs. III A and III B, the interfacial flow characteristics and the instability mechanisms for the transition between jetting and dripping modes can be understood in depth.

IV. CONCLUSIONS

The interfacial instability and the jetting-dripping transition in co-flow focusing process are studied through experiments, numerical simulations, and theoretical analysis. In experiments, a stable coaxial liquid cone can be established under moderate liquid flow rates, and the dripping and jetting modes of interface breakup downstream the focusing orifice can be observed. The experimental and numerical results show that the interface breakup can gradually transfer from dripping mode to jetting mode as the flow rates of core, shell, and driving liquid increase. The phase diagram of jetting and dripping modes is plotted. Through comparing the breakup of single outer jet to the coaxial liquid jets, it is found that the transition from jetting to dripping modes is triggered by the instability of the inner jet interface. The mode transition is studied through dimensional analysis of the local inner jet. The numerical results enable the accurate measurement of the diameter and velocity of inner jet, which indicates that the jet inertia force and the viscous shear stress would act corporately to maintain

a stable jet, and the transition from jetting to dripping modes is caused by the dominance of interfacial tension over the join forces of jet inertia and shear stress. Based on the velocity profiles obtained through numerical simulations, the linear spatiotemporal instability analysis of the coaxial jets is carried out, which predicts the effect of process parameters on jet instability and the transition boundaries of absolute/convective instability. The theoretical instability boundary agrees well with the experimental and numerical results. The energy budget analysis on the coaxial jets further suggests that the interfacial tension of inner jet provides main contribution to the coaxial jet instability and the transition from jetting to dripping modes. This study provides guidance for understanding the transition criterion of jetting and dripping modes in co-flow focusing, which has great significance for guiding the fabrication of compound droplets by the co-flow focusing technique in potential applications.

APPENDIX: THE EXPRESSIONS INVOLVED IN THE ENERGY BUDGET

For the inner jet,

$$KE_1 = \frac{2\pi}{T\lambda} \int_0^T \int_0^{\kappa_1} \int_0^{\lambda} \left(\frac{\partial}{\partial t} + U_1 \frac{\partial}{\partial z} \right) \left(\frac{u_1^2 + v_1^2}{2} \right) r \, dz \, dr \, dt,$$

$$REY_1 = -\frac{2\pi}{T\lambda} \int_0^T \int_0^{\kappa_1} \int_0^{\lambda} v_1 u_1 \frac{\partial U_1}{\partial r} r \, dz \, dr \, dt,$$

$$PRL_{1s} = -\frac{2\pi}{T\lambda S} \int_0^T \int_0^{\lambda} (v_1 p_2)_{r=\kappa_1} \kappa_1 \, dz \, dt,$$

$$NVL_{1s} = \frac{2\pi}{T\lambda S Re} \int_0^T \int_0^{\lambda} \left[2v_1 \frac{\partial v_2}{\partial r} \right]_{r=\kappa_1} \kappa_1 \, dz \, dt,$$

$$SUT_1 = \frac{2\pi}{T\lambda S} \int_0^T \int_0^{\lambda} \left[\frac{\sigma_{12}}{We} v_1 \left(\frac{\partial^2}{\partial z^2} + \frac{1}{\kappa_1^2} \right) \eta_1 \right]_{r=\kappa_1} \kappa_1 \, dz \, dt,$$

$$PRL_{1r} = -\frac{2\pi}{T\lambda S} \int_0^T \int_0^{\kappa_1} [u_1 p_1]_{z=0}^{z=\lambda} r \, dr \, dt,$$

$$SHL_{1r} = \frac{2\pi}{T\lambda Re_1} \int_0^T \int_0^{\kappa_1} v_1 \left[\frac{\partial u_1}{\partial r} + \frac{\partial v_1}{\partial z} \right]_{z=0}^{z=\lambda} r \, dr \, dt,$$

$$NVL_{1r} = \frac{2\pi}{T\lambda Re_1} \int_0^T \int_0^{\kappa_1} \left[2u_1 \frac{\partial u_1}{\partial r} \right]_{z=0}^{z=\lambda} r \, dr \, dt,$$

$$SHB_1 = \frac{2\pi}{T\lambda Re_1} \int_0^T \int_0^{\lambda} u_1 \eta_1 \left(\frac{1}{N} \frac{d^2 U_2}{dr^2} - \frac{d^2 U_1}{dr^2} \right)_{r=\kappa_1} \kappa_1 \, dz \, dt,$$

$$SHL_{1s} = \frac{2\pi}{T\lambda Re_1 N} \int_0^T \int_0^{\lambda} \left[u_1 \left(\frac{\partial u_2}{\partial r} + \frac{\partial v_2}{\partial z} \right) \right]_{r=\kappa_1} \kappa_1 \, dz \, dt,$$

$$DIS_1 = -\frac{2\pi}{T\lambda Re_1}\int_0^T\int_0^{\kappa_1}\int_0^\lambda\left[2\left(\frac{\partial v_1}{\partial r}\right)^2 + 2\left(\frac{\partial u_1}{\partial z}\right)^2\right.$$
$$\left. + 2\left(\frac{v_1}{r}\right)^2 + \left(\frac{\partial u_1}{\partial r} + \frac{\partial v_1}{\partial z}\right)^2\right] r\,\mathrm{d}z\mathrm{d}r\mathrm{d}t.$$

For the outer jet,

$$KE_2 = \frac{2\pi}{T\lambda}\int_0^T\int_{\kappa_1}^1\int_0^\lambda\left(\frac{\partial}{\partial t} + U_2\frac{\partial}{\partial z}\right)\left(\frac{u_2^2 + v_2^2}{2}\right)r\,\mathrm{d}z\mathrm{d}r\mathrm{d}t,$$

$$REY_2 = -\frac{2\pi}{T\lambda}\int_0^T\int_{\kappa_1}^1\int_0^\lambda v_2 u_2\frac{dU_2}{dr}r\,\mathrm{d}z\mathrm{d}r\mathrm{d}t,$$

$$PRL_{2s} = \frac{2\pi}{T\lambda}\int_0^T\int_0^\lambda[v_2 p_2]_{r=\kappa_1}\kappa_1\,\mathrm{d}z\mathrm{d}t - \frac{2\pi}{T\lambda}\int_0^T\int_0^\lambda(v_2 p_3)_{r=1}\,\mathrm{d}z\mathrm{d}t,$$

$$NVL_{2s} = \frac{2\pi M}{T\lambda Re}\int_0^T\int_0^\lambda\left[2v_2\frac{\partial v_3}{\partial r}\right]_{r=1}\mathrm{d}z\mathrm{d}t,$$

$$SUT_2 = \frac{2\pi}{T\lambda}\int_0^T\int_0^\lambda\frac{1}{We}\left[v_2\left(\frac{\partial^2}{\partial z^2} + 1\right)\eta_2\right]_{r=1}\mathrm{d}z\mathrm{d}t,$$

$$PRL_{2r} = -\frac{2\pi}{T\lambda}\int_0^T\int_{\kappa_1}^1[u_2 p_2]_{z=0}^{z=\lambda}r\,\mathrm{d}r\mathrm{d}t,$$

$$SHL_{2r} = \frac{2\pi}{T\lambda Re}\int_0^T\int_{\kappa_1}^1\left[v_2\left(\frac{\partial u_2}{\partial r} + \frac{\partial v_2}{\partial z}\right)\right]_{z=0}^{z=\lambda}r\,\mathrm{d}r\mathrm{d}t,$$

$$NVL_{2r} = \frac{2\pi}{T\lambda Re}\int_0^T\int_{\kappa_1}^1\left[2u_2\frac{\partial u_2}{\partial z}\right]_{z=0}^{z=\lambda}r\,\mathrm{d}r\mathrm{d}t,$$

$$SHB_2 = \frac{2\pi}{T\lambda Re}\int_0^T\int_0^\lambda u_2\eta_2\left(M\frac{d^2 U_3}{dr^2} - \frac{d^2 U_2}{dr^2}\right)_{r=1}\mathrm{d}z\mathrm{d}t,$$

$$SHL_{2s} = \frac{2\pi}{T\lambda Re}\int_0^T\int_0^\lambda M u_2\left(\frac{\partial u_3}{\partial r} + \frac{\partial v_3}{\partial z}\right)_{r=1}\mathrm{d}z\mathrm{d}t$$
$$- \frac{2\pi}{T\lambda Re}\int_0^T\int_0^\lambda\left[u_2\left(\frac{\partial u_2}{\partial r} + \frac{\partial v_2}{\partial z}\right)\right]_{r=\kappa_1}\kappa_1\,\mathrm{d}z\mathrm{d}t,$$

$$DIS_2 = -\frac{2\pi}{T\lambda Re}\int_0^T\int_{\kappa_1}^1\int_0^\lambda\left[2\left(\frac{\partial v_2}{\partial r}\right)^2 + 2\left(\frac{\partial u_2}{\partial z}\right)^2 + 2\left(\frac{v_2}{r}\right)^2\right.$$
$$\left. + \left(\frac{\partial u_2}{\partial r} + \frac{\partial v_2}{\partial z}\right)^2\right] r\,\mathrm{d}z\mathrm{d}r\mathrm{d}t.$$

DATA AVAILABILITY

The data that support the findings of this study are available from the corresponding author upon reasonable request.

REFERENCES

[1]A. Barrero and I. G. Loscertales, "Micro- and nanoparticles via capillary flows," Annu. Rev. Fluid Mech. **39**, 89–106 (2007).

[2]S. L. Anna, "Droplets and bubbles in microfluidic devices," Annu. Rev. Fluid Mech. **48**, 285–309 (2016).

[3]A. M. Gañán-Calvo, "Generation of steady liquid microthreads and micronsized monodisperse sprays in gas streams," Phys. Rev. Lett. **80**, 285–288 (1998).

[4]A. M. Gañán-Calvo, J. M. Montanero, L. Martin-Banderas, and M. Flores-Mosquera, "Building functional materials for health care and pharmacy from microfluidic principles and flow focusing," Adv. Drug Delivery Rev. **65**, 1447–1469 (2013).

[5]M. A. Herrada, J. M. Montanero, C. Ferrera, and A. M. Gañán-Calvo, "Analysis of the dripping-jetting transition in compound capillary jets," J. Fluid Mech. **649**, 523–536 (2010).

[6]T. Si, G. B. Li, Q. Wu, Z. Q. Zhu, X. S. Luo, and R. X. Xu, "Optical droplet vaporization of nanoparticle-loaded stimuli-responsive microbubbles," Appl. Phys. Lett. **108**, 111109 (2016).

[7]K. Mu, H. Ding, and T. Si, "Experimental and numerical investigations on interface coupling of coaxial liquid jets in co-flow focusing," Phys. Fluids **32**, 042103 (2020).

[8]K. Mu, G. B. Li, and T. Si, "Instability and interface coupling of coaxial liquid jets in a driving stream," Phys. Fluids **32**, 092107 (2020).

[9]J. Montanero and A. M. Gañán-Calvo, "Dripping, jetting and tip streaming," Rep. Prog. Phys. **83**, 097001 (2020).

[10]A. S. Utada, E. Lorenceau, D. R. Link, P. D. Kaplan, H. A. Stone, and D. A. Weitz, "Monodisperse double emulsions generated from a microcapillary device," Science **308**, 537–541 (2005).

[11]Z. Nie, S. Xu, M. Seo, P. C. Lewis, and E. Kumacheva, "Polymer particles with various shapes and morphologies produced in continuous microfluidic reactors," J. Am. Chem. Soc. **127**, 8058–8063 (2005).

[12]A. Evangelio, F. Campo-Cortes, and J. M. Gordillo, "Simple and double microemulsions via the capillary breakup of highly stretched liquid jets," J. Fluid Mech. **804**, 550–577 (2016).

[13]J. Guerrero, Y. W. Chang, A. A. Fragkopoulos, and A. Fernandez-Nieves, "Capillary-based microfluidics-coflow, flow-focusing, electro-coflow, drops, jets, and instabilities," Small **16**, 1904344 (2020).

[14]T. Si, F. Li, X. Y. Yin, and X. Z. Yin, "Modes in flow focusing and instability of coaxial liquid-gas jets," J. Fluid Mech. **629**, 1–23 (2009).

[15]A. M. Gañán-Calvo and P. Riesco-Chueca, "Jetting-dripping transition of a liquid jet in a lower viscosity co-flowing immiscible liquid: The minimum flow rate in flow focusing," J. Fluid Mech. **553**, 75–84 (2006).

[16]M. A. Herrada, A. M. Gañán-Calvo, and A. Ojeda-Monge, "Liquid flow focused by a gas: Jetting, dripping, and recirculation," Phys. Rev. E **78**, 036323 (2008).

[17]C. Y. Yang, R. Qiao, K. Mu, Z. Q. Zhu, R. X. Xu, and T. Si, "Manipulation of jet breakup length and droplet size in axisymmetric flow focusing upon actuation," Phys. Fluids **31**, 091702 (2019).

[18]K. Mu, T. Si, E. Q. Li, R. X. Xu, and H. Ding, "Numerical study on droplet generation in axisymmetric flow focusing upon actuation," Phys. Fluids **30**, 012111 (2018).

[19]A. M. Gañán-Calvo, M. A. Herrada, and P. Garstecki, "Bubbling in unbounded coflowing liquids," Phys. Rev. Lett. **96**, 124504 (2006).

[20]T. X. Zhang, X. Zou, L. Xu, D. W. Pan, and W. X. Huang, "Numerical investigation of fluid property effects on formation dynamics of millimeter-scale compound droplets in a co-flowing device," Chem. Eng. Sci. **229**, 116156 (2021).

[21]X. D. Liu, L. Y. Wu, Y. J. Zhao, and Y. P. Chen, "Study of compound drop formation in axisymmetric microfluidic devices with different geometries," Colloids Surf., A **533**, 87–98 (2017).

[22]S. A. Nabavi, S. Gu, G. T. Vladisavljević, and E. E. Ekanem, "Dynamics of double emulsion break-up in three phase glass capillary microfluidic devices," J. Colloid Interface Sci. **450**, 279–287 (2015).

[23]Y. P. Chen, L. Y. Wu, and L. Zhang, "Dynamic behaviors of double emulsion formation in a flow-focusing device," Int. J. Heat Mass Transfer **82**, 42–50 (2015).

[24]J. Eggers and E. Villermaux, "Physics of liquid jets," Rep. Prog. Phys. **71**, 036601 (2008).

[25]E. J. Vega, J. M. Montanero, M. A. Herrada, and A. M. Gañán-Calvo, "Global and local instability of flow focusing: The influence of the geometry," Phys. Fluids **22**, 064105 (2010).

[26]A. Chauhan, C. Maldarelli, D. T. Papageorgiou, and D. S. Rumschitzki, "Temporal instability of compound threads and jets," J. Fluid Mech. **420**, 1–25 (2000).

[27]D. Jacqmin, "Calculation of two-phase Navier–Stokes flows using phase-field modeling," J. Comput. Phys. **155**, 96–127 (1999).

[28]H. Ding, P. D. M. Spelt, and C. Shu, "Diffuse interface model for incompressible two-phase flows with large density ratios," J. Comput. Phys. **226**, 2078–2095 (2007).

[29]K. Mu, H. Ding, and T. Si, "Instability analysis of the cone-jet flow in liquid-driven flow focusing," Microfluid. Nanofluid. **22**, 138 (2018).

[30]K. Mu, T. Si, and H. Ding, "Nonlinear dynamics and manipulation of dripping in capillary flow focusing," Sci. China: Phys., Mech. Astron. **62**, 124713 (2019).

[31]S. P. Lin and J. N. Chen, "Role played by the interfacial shear in the instability mechanism of a viscous liquid jet surrounded by a viscous gas in a pipe," J. Fluid Mech. **376**, 37–51 (1998).

[32]F. Li, X. Y. Yin, and X. Z. Yin, "Axisymmetric and non-axisymmetric instability of an electrified viscous coaxial jet," J. Fluid Mech. **632**, 199–225 (2009).

[33]J. P. Matas, A. Delon, and A. Cartellier, "Shear instability of an axisymmetric air-water coaxial jet," J. Fluid Mech. **843**, 575–600 (2018).

[34]K. Mu, R. Qiao, J. F. Guo, C. Y. Yang, Y. F. Wu, and T. Si, "Parametric study on stability and morphology of liquid cone in flow focusing," Int. J. Multiphase Flow **135**, 103507 (2021).

[35]A. S. Utada, A. Fernandez-Nieves, H. A. Stone, and D. A. Weitz, "Dripping to jetting transition in coflowing liquid streams," Phys. Rev. Lett. **99**, 094502 (2007).

[36]C. F. Zhou, P. T. Yue, and J. J. Feng, "Formation of simple and compound drops in microfluidic devices," Phys. Fluids **18**, 092105 (2006).

[37]T. Si, H. X. Feng, X. S. Luo, and R. X. Xu, "Formation of steady compound cone-jet modes and multilayered droplets in a tri-axial capillary flow focusing device," Microfluid. Nanofluid. **18**, 967–977 (2015).

[38]P. Huerre and P. A. Monkewitz, "Local and global instabilities in spatially developing flows," Annu. Rev. Fluid Mech. **22**, 473–537 (1990).

[39]A. K. R. K. Kupfer and A. Bers, "The cusp map in the complex-frequency plane for absolute instabilities," Phys. Fluids **30**, 3075–3082 (1987).